V. HALDAR ⊙[1*], S. PAL ⊙[1]

# A METALLURGICAL STUDY OF MICRO PLASMA ARC WELDED JOINT OF AUSTENITIC STAINLESS-STEEL BLANK

Micro plasma arc welding (MPAW) is frequently used for joining thin sheets of ferrous and nonferrous materials. In this study, austenitic stainless steel 316L of 0.5 mm thin sheets are joined by using MPAW. The weld metallurgy is characterized by field electron scanning microscopy (FESEM), Transmission electron microscopy (TEM), and X-ray diffraction (XRD) techniques to evaluate different phases formation and their orientation in detail. Mechanical tests like tensile test, micro hardness test is also carried out to measure the joint quality. It is found that the weld joint is constituent of two major phases, $\delta$-ferrite and austenite ($\gamma$), and few secondary phases like chromium carbides. The ferrite percentage in the fusion zone is higher than the as received base material. The fusion zone hardness is increased due to the presence of high amount of ferrite and carbides. The tensile fracture surface contains lots of dimples and voids, which indicates good ductility of the joint. A defect free and good joint efficiency is achieved by using MPAW.

*Keywords:* Micro plasma arc welding; TEM analysis; Austenitic; 316L stainless steel; Tensile test

## 1. Introduction

Austenitic stainless-steel (ASS) 316L is a low carbon (~0.03%) stainless steel which consist of two major phases like FCC austenite ($\gamma$) and BCC $\delta$-ferrite. Due to low carbon this steel is generally used where inter granular corrosion and inter granular attack resistivity is required [1]. It contains 16-18% Cr which helps in increasing its corrosion resistance [2]. Moreover, it has superior properties like good weldability and creep behavior at the elevated temperature and formability. Thus, it is used in the fabrication of mechanical bellow, car exhaust system and food processing industries [3,4]. Different types of welding techniques are employed to join these steel sheets. However, due to the welding operation there is a chance of joint failure specially for thin sheets due to the microstructural variation, induced residual stresses [5,6] and variation of temperature gradient. Hence, it is important to choose a proper welding technique to join these sheets. Electron beam welding and laser welding are the most advanced welding techniques for the joining of thin sheets. However, these welding techniques have some constraints in overall setup cost and large geometry. On the other hand, tungsten inert gas welding (TIG) is a low cost welding process but it has a limitation to join thin (<1 mm) sheet due to burn

through of the sheet. MPAW is able to joint ultra-thin sheet up to 0.1 mm without leaving any defect due to high concentrated energy density and stable arc at a minimum current range up to 1 A [7,8]. In MPAW a pure argon gas is used, which has two purposes i.e., the shielding and the plasma generation. The shielding gas helps to reduce the formation of oxides during the welding process. Numerous authors have studied similar and dissimilar MPAW of SS 316L numerically and experimentally [9,10]. Saha et al. [11] studied on high cycle fatigue behavior of SS 316L and observed that higher quantity of $\delta$-ferrite is the main responsible for the fatigue failure. Chaudhary et al. [12] optimized the joint strength of pulsed MPAW of ASS 316L. They concluded that the welded joint has insignificant heat affected zone due to low peak current and the fusion zone (FZ) hardness is higher than the parent material. Dwibedi et al. [10] experimented on dissimilar thickness tailored welded blank (WB) of ASS 316L and explained the effect of welding speed, stand of distance (SOD) and welding current on joint strength. It was found that there is absence of HAZ due to low and concentrated heat input during MPAW [13].

Based on the previous work it is overserved that many authors have studied the MPAW of ASS 316L. Most of them put their efforts to determine the effect of process parameters on

1    INDIAN INSTITUTE OF TECHNOLOGY, GUWAHATI, INDIA

*    Corresponding author: vivek176103115@iitg.ac.in

the joint strength. However, less literatures are found on metallurgical variations due to MPAW that causes failure during the application. Present work studies on thin (0.5 mm) ASS 316L sheet joining using micro plasma arc welding. The microstructural changes, presence of different secondary phases and their effect on mechanical properties are explained in details.

## 2. Experimental Procedure

ASS 316L sheets with dimension of 110 mm length, 60 mm width and 0.5 mm thick are butt welded using MPAW (make: EWM). The ASS 316L base material (BM) composition is evaluated by energy dispersive X-ray (EDS) analysis and represented in TABLE 1. The welding parameters are decided from the previous study [14] and shown in TABLE 2. In this experiment the workpiece is moved at a constant velocity beneath the plasma torch. Figs. 1(a) and 1(b) represent the plasma torch and copper fixture, respectively. Copper fixture helps to reduce the chance of defects formation like distortion and residual stress caused by heat accumulation inside the work piece at the time of welding. A small specimen is cut at the center of the WB for the metallurgical study. Thereafter, the specimen is mirror polished using different grade emery papers, velvet cloth with fine alumina powder (0.3 μm) and finally etched by nitric acid, glycerol and hydrochloric acid (5:10:15) mixture. The micro graph of the etched specimen is taken by optical microscope and FESEM (Make: Zeiss; Model: sigma) equipped with EDS (Make: Oxford). The phases present in the FZ and BM is determined by XRD (Make: Rigaku Technologies; Model: Smartlab) and TEM (Make- JEOL, 2100F) analysis. For TEM analysis a thin (<100 μm) 3 mm disc is prepared and electro polished in (9:1) perchloric acid and water medium. The micro hardness values at the cross section of the FZ and base zone (BZ) are measured by Vickers micro hardness tester (Make: Buehler; Model: Micrometer-2101).

TABLE 1

Constituent alloying elements of as received BM (wt.%)

| Material | Mo | Si | Ni | Mn | Cr | Co | S | W | Fe |
|---|---|---|---|---|---|---|---|---|---|
| ASS 316L | 2.07 | 0.51 | 10.2 | 1.41 | 16.98 | 0.03 | 0.02 | 0.15 | Bal. |
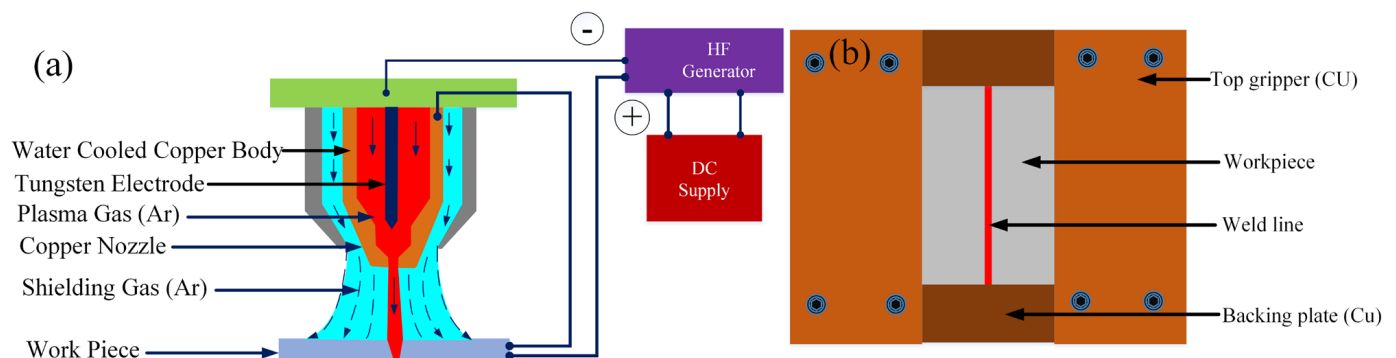
The tensile samples are prepared according to ASTM E8 [15] sub size standard (25 mm gauge length) and the test is carried out in a Universal tensile testing machine (Biss-250 kN) with constant cross head speed of 1 mm/min. The fracture surface of the tensile specimen is also studied to determine the nature of failure.

TABLE 2

Welding parameters

| Parameters | Value |
|---|---|
| Welding speed (mm/s) | 3.5 |
| Current (A) | 9.5 |
| Stand of distance (mm) | 1.5 |
| Plasma gas flow rate (LPM) | 0.6 |
| Shielding gas flow rate (LPM) | 5.0 |
| Nozzle orifice diameter (mm) | 1.0 |
| Electrode diameter (mm) | 3.5 |

## 3. Results and discussion

### 3.1. Microstructural analysis

The as received BM microstructure is represented in Fig. 2(a-b), it consists of fine dense equiaxed grains (~12.5 μm) with annealing twins. It is also observed from the Fig. 2(b) that the γ-matrix is the main constituent phase in ASS 316L BM upon which the δ-ferrite are distributed at the grain boundaries. The δ-ferrite are formed due to the segregation of ferrite stimulating elements like Cr at the time of solidification or thermal and mechanical treatment.

Fig. 3(a-e) represents the macro view of the weld cross section and microstructural variation of different locations of the FZ. A clear transition zone (TZ) is observed which separates the BZ and FZ. The magnified FESEM image of the TZ is reprsented in Fig. 3(c), in which an epitaxial type grain growth is observed due to the presence of multiple alloying elements in the alloy [16]. However, there is no grain refinement or enlargement is observed at the HAZ due to lower amount of heat input and fast cooling by the copper backing plate during the welding process. As a result of this a narrow (~120 μm) HAZ is observed both side of the FZ. Fig. 3(d-e) illustrates the presence of two distinct structures of δ-ferrite in the FZ, namely skeletal and lathy δ-ferrite.



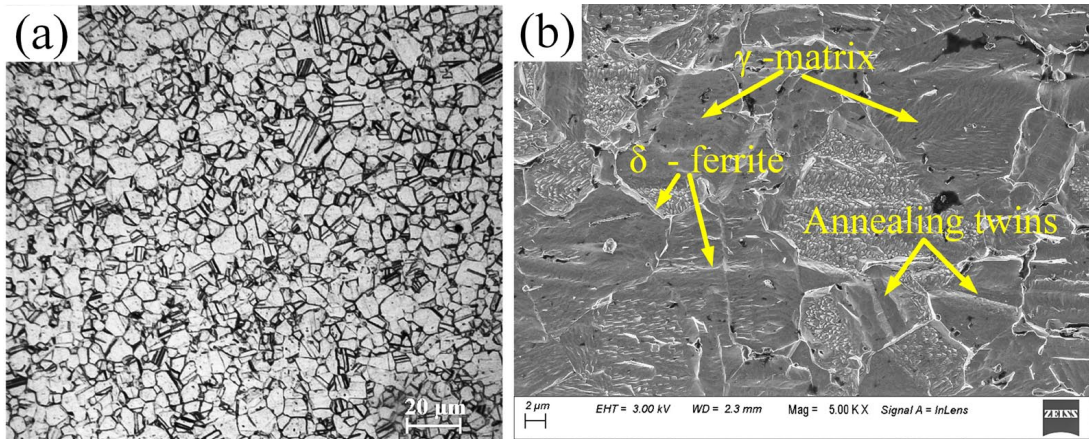Fig. 1. Schematic of (a) MPAW nozzle (b) copper fixture

Fig. 2. Micrograph of the BM (a) optical image and (b) magnified FESEM image
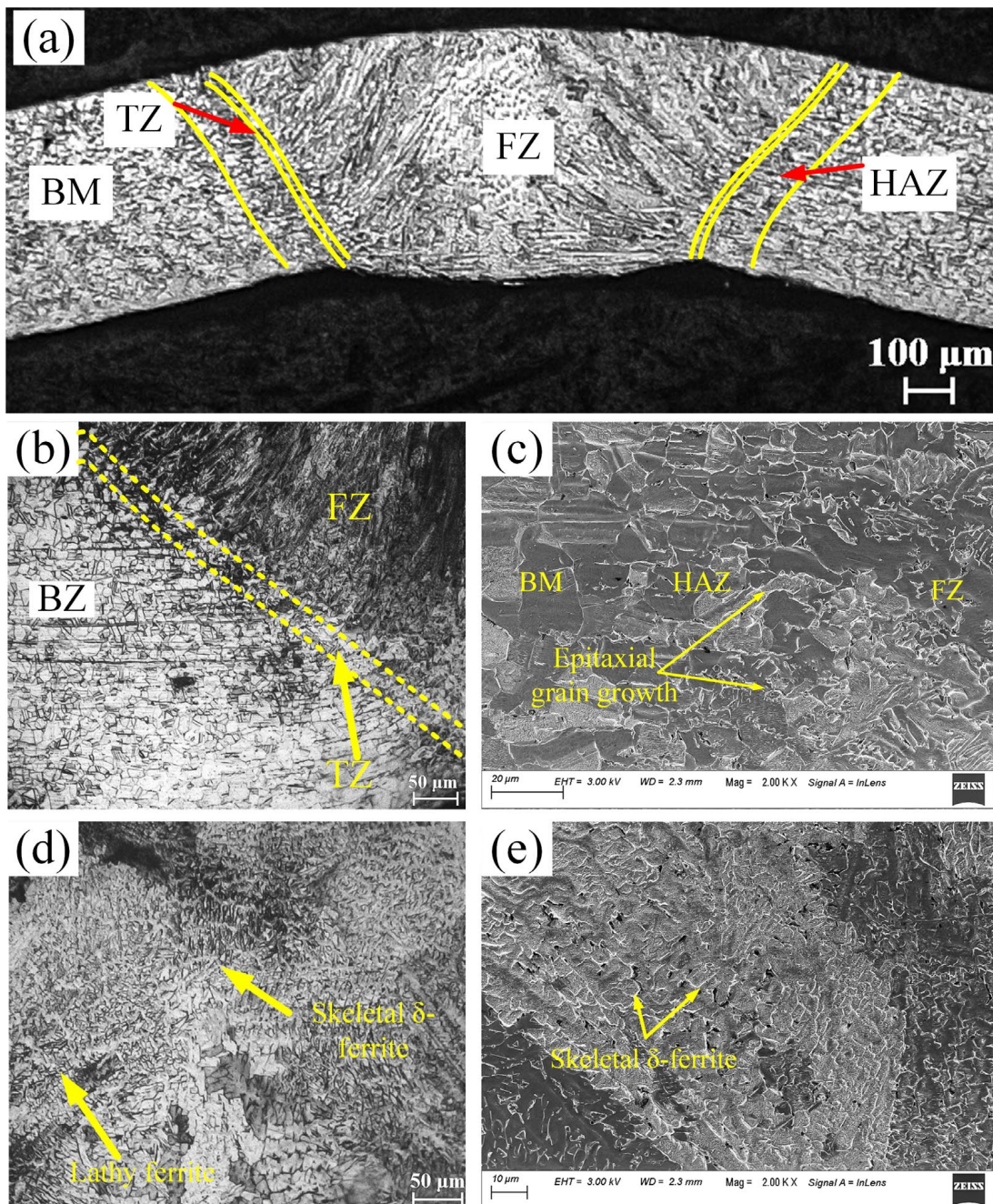


Fig. 3. (a) Macro view of the weld cross section (b) Optical (c) FESEM image of TZ and (d) optical (e) FESEM images of FZ

The formation of these different ferrite structure in the FZ can be predicted by using chemical composition dependent diagram (Fig. 4(a)). The ratio of Chromium $[Cr]_{Eq}$ and nickel equivalent $[Ni]_{Eq}$ indicates the the mode of solidification. The $[Cr]_{Eq}$ and $[Ni]_{Eq}$ is expressed as:

$$[Cr]_{Eq} = W_{Cr} + 1.5W_{Si} + 0.5W_{Nb} + 2W_{Ti} \qquad (1)$$

$$[Ni]_{Eq} = W_{Ni} + 30W_{C} + 0.5_{Mn} \qquad (2)$$

To measure the $[Cr]_{Eq}$ and $[Ni]_{Eq}$, the chemical composition of the FZ is measured by EDS analysis and tabulated in TABLE 2. It is found as $[Cr]_{Eq}$ = 19.87 and $[Ni]_{Eq}$ = 12.93. Hence, the ratio is, $[Cr]_{Eq}/[Ni]_{Eq}$ = 1.53. According to Fig. 4(a) this ratio indicates the mode solidification as FA mode, where F and A indicates as ferrite and austenite. In the FA mode solidification, some $\gamma$ forms at the end of solidification due to peritectic-eutectic reaction, which deposited solidification boundaries of ferrite [1]. As a result of this two types of ferrite are formed at the time of MPAW. The intersection point of $[Cr]_{Eq}$ and $[Ni]_{Eq}$ is represented on the Schaeffler diagram in Fig. 4(b) [17]. It can be observed that the percentage of ferrite at the FZ is more than 6%.

The volume percentage of ferrite in the BZ and FZ is also measured by ImageJ software using color thresold tool, shown in Fig. 5(a-b). It has been found that the FZ contains a higher percentage of ferrite than the others region of the WB. At the early stage of weld pool solidification, $\delta$-ferrite is formed, and after that, it transforms to $\gamma$. However, due to fast cooling, this $\delta$-ferrite does not get sufficient time to transform into $\gamma$ fully and retained in the FZ. Thus, the percentage of $\delta$-ferrite in the FZ is increased sharply.

TABLE 3

Chemical composition of FZ

| Si | C | Mo | Ni | Cr | Mn | Ti |
|---|---|---|---|---|---|---|
| 0.5 | 0.031 | 1.8 | 11.0 | 17.3 | 2.0 | 0.01 |

The EDS elemental mapping is performred to identify the elemental distribution at the FZ (Fig. 6). A uniform elemental distribution is observed through out the FZ. However, the percentage of Cr and Ni at the grain boundaries are quite higher than the other locations. During the solidification this alloying
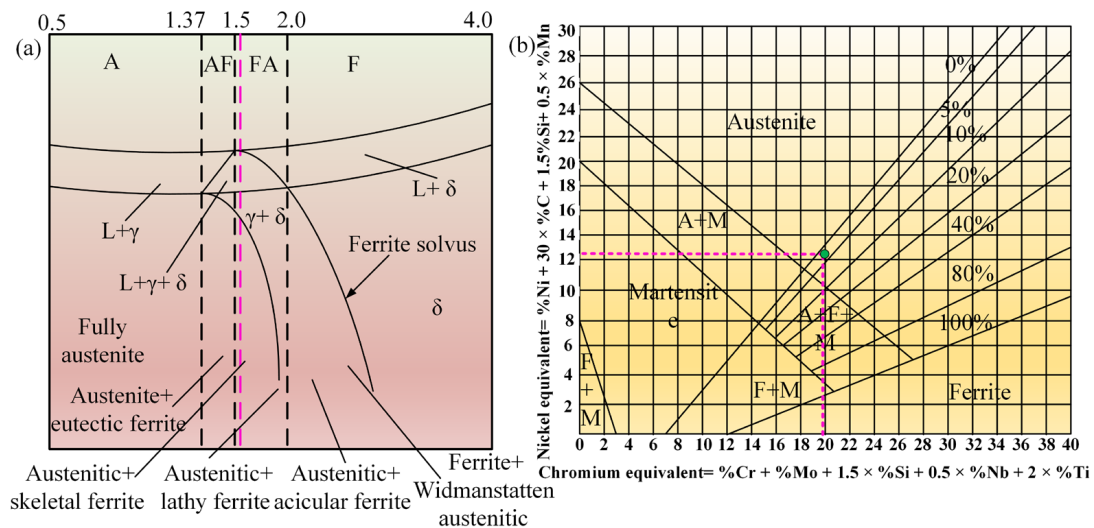


Fig. 4. (a) Solidification modes of ASS 316L based on chemical composition and (b) Schaeffler diagram
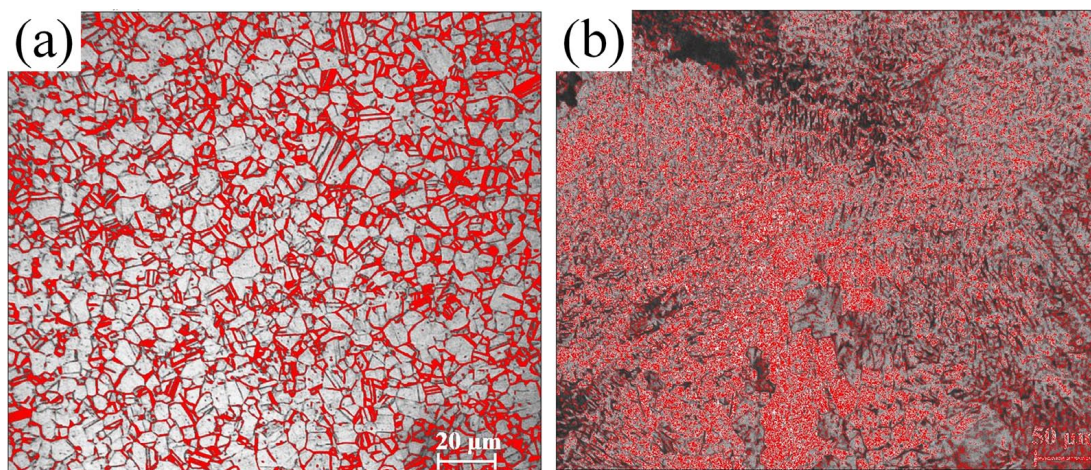


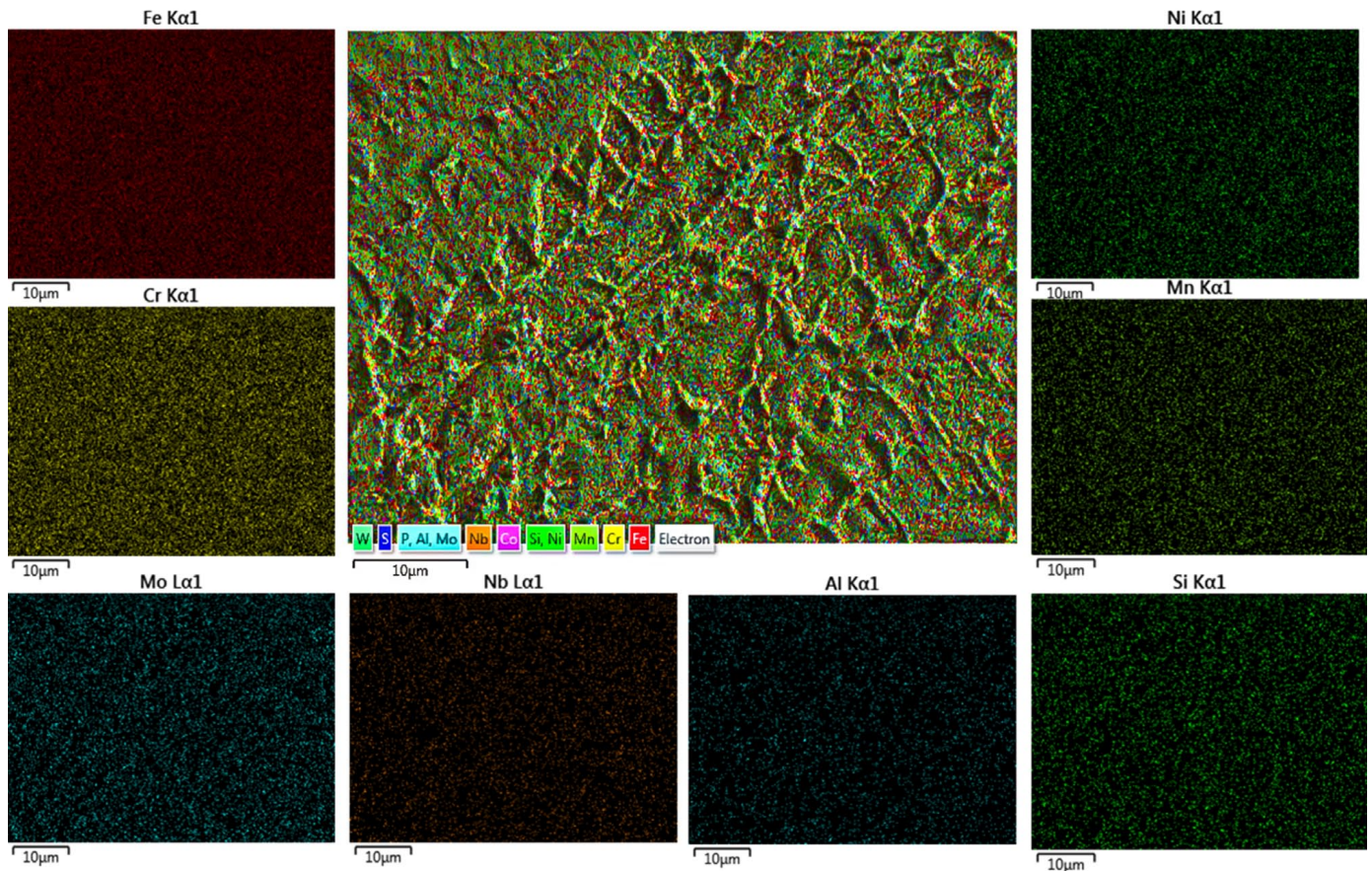Fig. 5. Color threshold for ferrite percentage in (a) BZ and (b) FZ

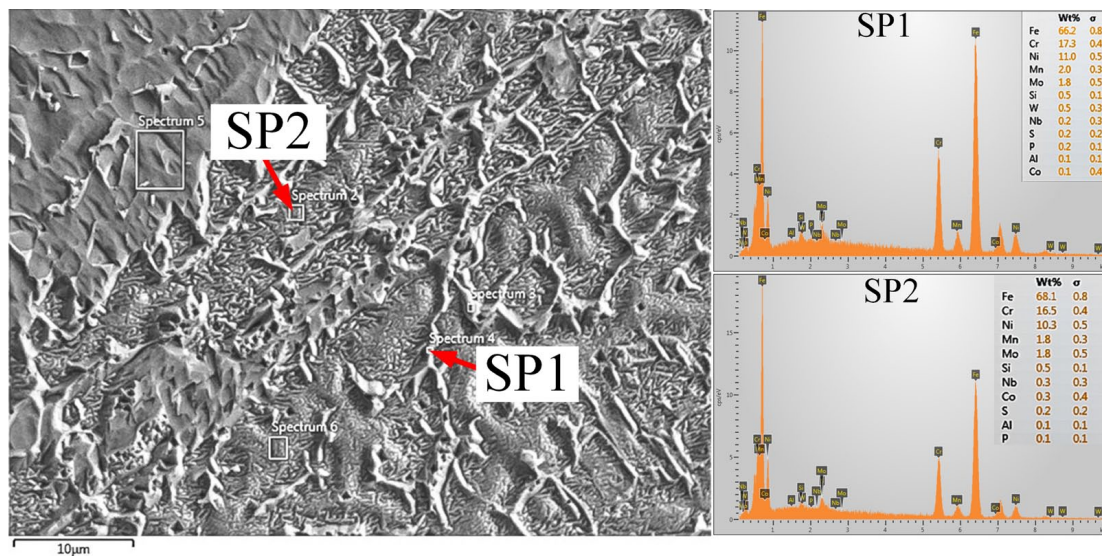Fig. 6. EDS elements mapping at the FZ



Fig. 7. Point analysis at different locations of the FZ

elements get segregated and deposited at the grain boundaries. An EDS point analysis is also carried out at several location in the FZ including dendritic and interdendritic regions to measure the weight percentage of the alloying elements and represented in Fig. 7. It is observed that the Cr and Ni percentage at the dendritic region is higher than the interdendritic region.

The presence of different phases at the FZ are identified using XRD analysis and the XRD pattern is represented in Fig. 8.

It is observed that $\gamma$ is the dominating phase which has maximum peak intensity in (111) plane at 43.47° angle. On the other hand, ferrite has low intensity as compared with the $\gamma$, which is located adjacent to the $\gamma$ at 44.62° angle in (110) plane. Cr-carbide, $Cr_7C_3$, is also detected at 44.22° angle in the plane of (124). However, there may be other secondary phases but due to low intensity, they are not observed in the XRD pattern. Hence, a TEM analysis is carried out to identify the secondary phases present at the FZ.

It is found from the TEM observation that the ferrite is embedded on the $\gamma$-matrix. In Fig. 8(a) the boundaries between the $\gamma$ and $\delta$ is not regular this is usual in austenitic stainless steel.
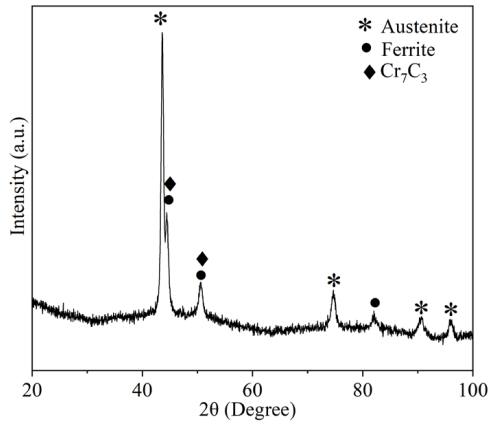


Fig. 8. XRD pattern of the FZ with different phases

The phases present is confirmed by Selected area diffraction (SAED), which indicates that the $\gamma$ is the main matrix, which has mainly three crystal orientation i.e., <200>, <211> and <220>. On the other hand, ferrite has <110> and <311> crystal orienta-

tion. Few tiny precipitates are also observed, shown in Fig. 9(b-c) and they are enriched Cr. A High-resolution transmission electron microscopy (HRTEM) is used at this zone and it is confirmed that those precipitates are chromium carbide ($Cr_7C_3$), shown in Fig. 10. A homogeneous dislocation density is observed on the $\gamma$-matrix, Fig. 8(d). At the time of solidification of the FZ, a thermal contraction is created between the $\delta$ and $\gamma$ and as a result the dislocations are formed.

### 3.2. Hardness test

The hardness value of the WB cross-section is measured and the obtained hardness profile is represented in Fig. 11. It can be observed that the FZ hardness (182.5±3.5) increases sharply with the comparion of BZ hardness (163.08±1.65). In the previous section it is confirmed that the FZ consist some carbide particles and high percentage of ferrite. As result the FZ hardness is found higher than other zones of the welded blank. However, there is a flactuation of the hardness value at the FZ center due to the presence of randomly distributed chromium carbide. It is also found that the HAZ hardness value (167.5±4.1) is slightly higher than the BZ, due to tempering during welding.
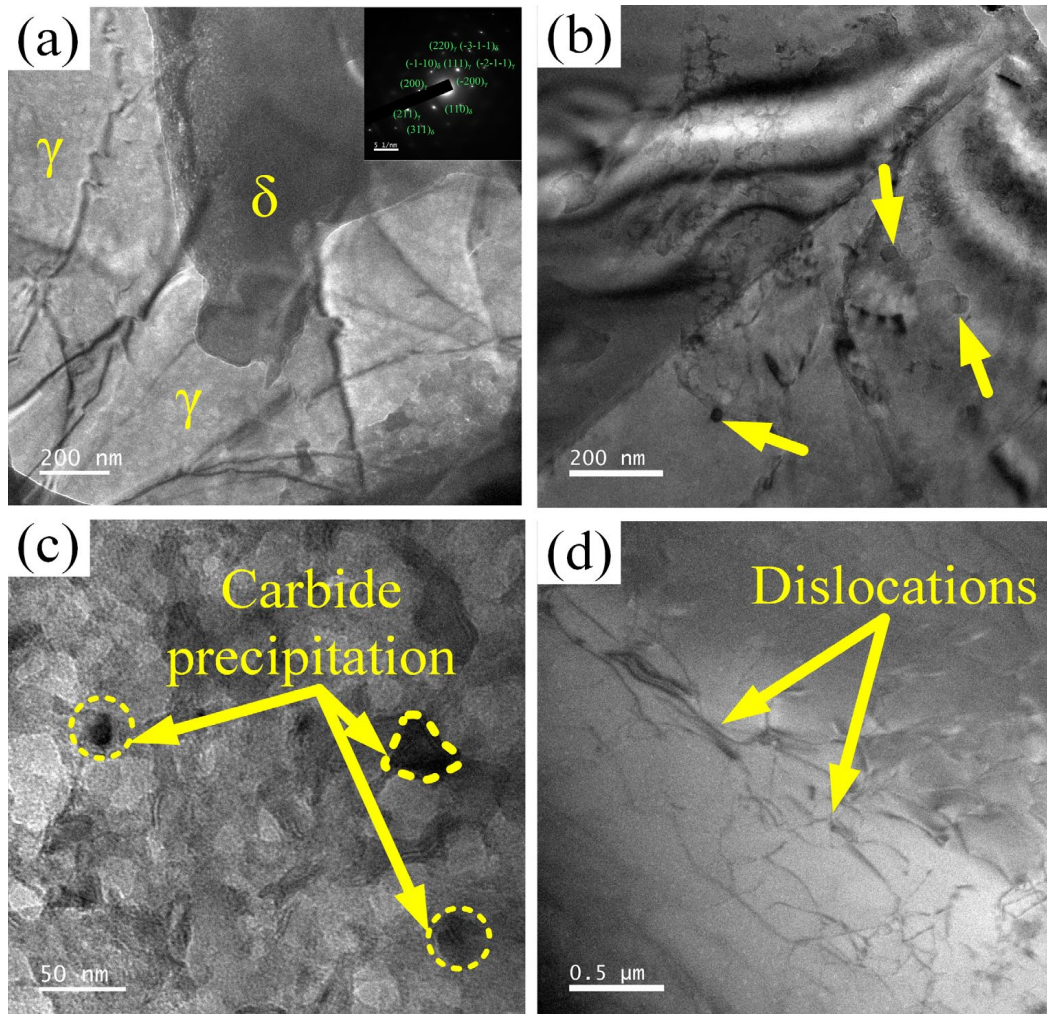


Fig. 9. TEM bright field image of (a) dislocation tangles (b-c) carbide particles and (d) dislocation density at the FZ
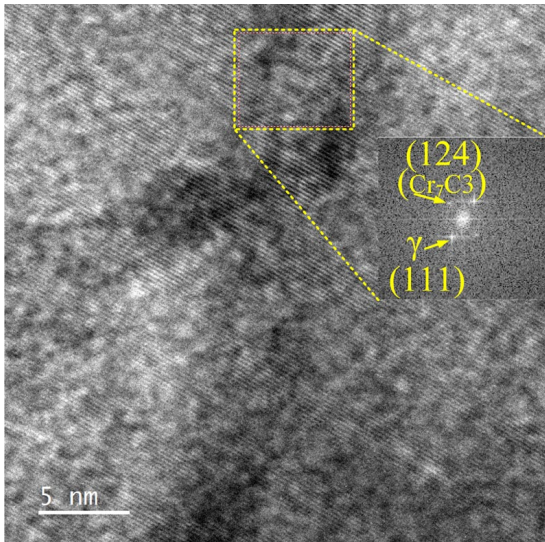
with the BM strength. Fig. 12(a) shows the stress-strain graph and TABLE 4 represents the tensile data. The maximum ultimate tensile strength (UTS) of the WB is found as 667.00 MPa, which is 97.46% of BM UTS. The measured elongation of the WB is 44.86%, which is 78.45% of the BM. As the FZ consists with higher percentage of $\delta$-ferrite and different types of carbide precipitation like $Cr_7C_3$, the weld joint loses its ductility and the WB fails from the center of the FZ (marked as color box). A fractography analysis is also carried for the tensile fracture surface of the WB, shown in Fig. 12(b). The fracture surface exhibits numerous deep dimples, voids, and micro voids, suggesting that the weld joint possesses favourable ductility. This indicates that the mode of failure is primarily ductile in nature [18].



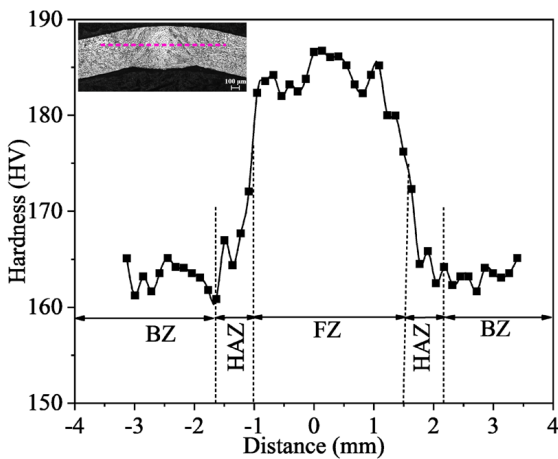Fig. 10. HRTEM analysis of precipitate area



Fig. 11. Hardness profile of the WB

### 3.3. Uniaxial tensile test

The joint strength of the autogenous micro plasma arc welded blank is evaluated by uniaxial tensile test and compared

TABLE 4

Uniaxial tensile properties of the BM and WB

| Sample | UTS (Mpa) | YS (Mpa) | Elongation (%) | n-value | K-value (Mpa) |
|---|---|---|---|---|---|
| BM | 684.70 ±10 | 289.16 ±10.3 | 57.20 ±12.34 | 0.39 ±0.05 | 1313.05 ±13.26 |
| WB | 667.0 ±7.5 | 318.4 ±7.72 | 44.87 ±8.36 | 0.37 ±0.07 | 1405.45 ±10.12 |

### 4. Conclusions

In this study, 0.5 mm thin ASS 316L sheets are butt welded successfully by using MPAW. Following are the major conclusions of the current study.

1. Two different skeletal and lathy $\delta$-ferrite are observed at the FZ. The volume percentage of ferrite at the FZ is higher than the BZ, as the FZ experiences rapid cooling at the time of solidification of the liquified weld pool. There is a narrow (~120 μm) HAZ is found due to low heat input.

2. The TEM analysis of the FZ reveals that it consists of different size of carbides precipitation. Which is confirmed as $Cr_3C_7$ by HRTEM analysis.

3. The FZ hardness is higher than the BM due to the presence of higher percentage of ferrite and carbide precipitation.
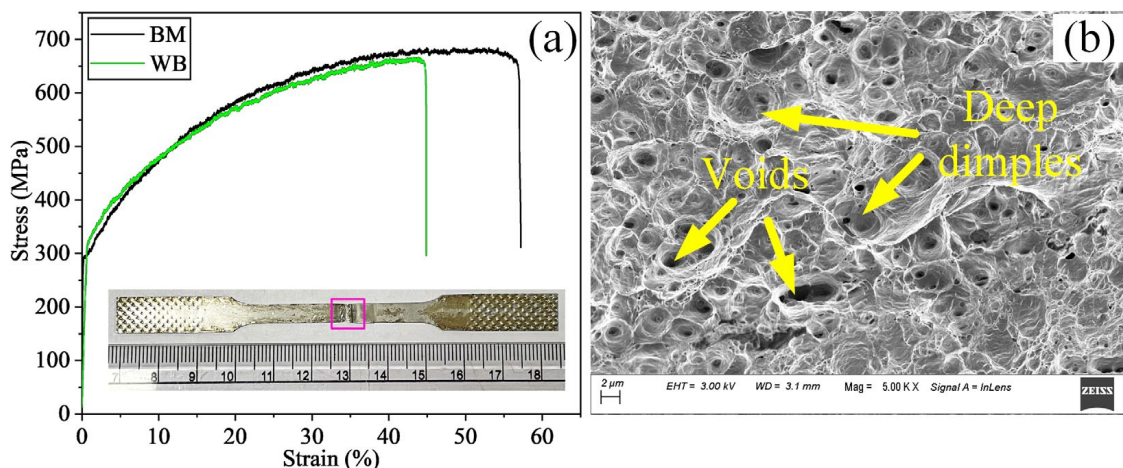


Fig. 12. (a) Engineering stress-strain data for the BM and WB and (b) Fractography of tensile fracture specimen of the WB

4.  It has been observed that the welded blank produced by MPAW exhibits excellent ductility, achieving a joint efficiency of over 90%.

## REFERENCES

[1]   J.C. Lippold, D.J. Kotecki, Welding Metallurgy and Weldability of Stainless Steels, 2005 John Wiley and Sons, New Jersey.

[2]   R. Sánchez-Tovar, M.T. Montañés, J. García-Antón, A. Guenbour, A. Ben-Bachir, Corrosion Behaviour of Micro-Plasma Arc Welded Stainless Steels in H3PO4 under Flowing Conditions at Different Temperatures. Corros. Sci. **53** (4), 1237-1246 (2011).

[3]   H. Chen, W. Li, Y.Y. Huang, Z. Xie, X. Zhu, B. Liu, B. Wang, Molten Pool Effect on Mechanical Properties in a Selective Laser Melting 316 L Stainless Steel at High-Velocity Deformation. Mater. Charact. **194**, 112409 (2022).

[4]   H. Dai, S. Shi, C. Guo, X. Chen, Stress Corrosion Cracking Behavior of 316 L SS in HF Vapor Environment Based on Corrosion Degradation as a Precursor. Corros. Sci. **208**, 110615 (2022).

[5]   X. Li, L. Hu, D. Deng, Influence of Contact Behavior on Welding Distortion and Residual Stress in a Thin-Plate Butt-Welded Joint Performed by Partial-Length Welding. Thin-Walled Struct. **176**, 109302 (2022).

[6]   S. Varmaziar, M. Atapour, Y.S. Hedberg, Corrosion and Metal Release Characterization of Stainless Steel 316L Weld Zones in Whey Protein Solution. NPJ Mater. Degrad. **6** (1), 1-9 (2022).

[7]   K.H. Tseng, S.T. Hsieh, C.C. Tseng, Effect of Process Parameters of Micro-Plasma Arc Welding on Morphology and Quality in Stainless Steel Edge Joint Welds. Sci. Technol. Weld. Join. **8** (6), 423-430 (2003).

[8]   D. Saha, S. Pal, Microstructure and Work Hardening Behavior of Micro-Plasma Arc Welded AISI 316L Sheet Joint. J. Mater. Eng. Perform. **28**, 2588-2599 (2019).

[9]   K.S. Prasad, C.S. Rao, D.N. Rao, Study on Weld Quality Characteristics of Micro Plasma Arc Welded Austenitic Stainless Steels. Procedia Eng. **97**, 752-757 (2014).

[10]  S. Dwibedi, S. Bag, Development of Micro-Plasma Arc Welding System for Different Thickness Dissimilar Austenitic Stainless Steels. J. Inst. Eng. Ser. C. **102** (3), 657-671 (2021).

[11]  D. Saha, S. Pal, Study on the Microstructural Variation and Fatigue Performance of Microplasma Arc Welded Thin 316L Sheet. Proc. Inst. Mech. Eng. Part L J. Mater. Des. Appl. **236** (4), 880-890 (2021).

[12]  J. Chaudhary, N.K. Jain, S. Pathak, S.C. Koria, Investigations on Thin SS Sheets Joining by Pulsed Micro-Plasma Transferred Arc Process. J. Micromanufacturing **2** (1), 15-24 (2019).

[13]  S. Dwibedi, N.K. Jain, S. Pathak, Investigations on Joining of Stainless Steel Tailored Blanks by M-PTA Process. Mater. Manuf. Process. **33** (16), 1851-1863 (2018).

[14]  V. Haldar, S.K. Biswal, S. Pal, Formability Study of Micro-Plasma Arc-Welded AISI 316L Stainless Steel Thin Sheet Joint. J. Brazilian Soc. Mech. Sci. Eng. **44** (11), 1-16 (2022).

[15]  ASTM Committee on Mechanical Testing. Standard Test Methods for Tension Testing of Metallic Materials. ASTM Int., ASTM Stds (Designation: E8/E8M-13a). 1-28 (2013).

[16]  S. Kou, Welding Metallurgy, 2003 John Wiley & Sons, New Jersey.

[17]  Y. Feng, Z. Luo, Z. Liu, Y. Li, Y. Luo, Y. Huang, Keyhole Gas Tungsten Arc Welding of AISI 316L Stainless Steel. Mater. Des. **85**, 24-31 (2015).

[18]  V. Haldar, S. Pal, Influence of Fusion Zone Metallurgy on the Mechanical Behavior of Ni-Based Superalloy and Austenitic Stainless Steel Dissimilar Joint. J. Mater. Eng. Perform. 1-19 (2023). DOI: https://doi.org/10.1007/s11665-023-08335-0